ChemComm

COMMUNICATION

View Article Online
View Journal | View Issue

Cite this: *Chem. Commun.*, 2023, 59, 4181

Received 26th December 2022,
Accepted 9th March 2023

DOI: 10.1039/d2cc07025a

rsc.li/chemcomm

Lipid droplet targeting-guided hypoxic photodynamic therapy with curcumin analogs†

Xuewei Li,[ab] Weimin Liu,*[ab] Xiuli Zheng,[ac] Meiyu Jiang,[ab] Yimin Guo,[ab] Jie Sha,[ab] Jiasheng Wu,[a] Haohui Ren,[ac] Honglei Gao,[ab] Shuai Wang[ab] and Pengfei Wang*[ab]

Two photosensitizers (CCOH and CCN) were designed and synthesized by introducing coumarin into the curcumin (CUR) structure. Compared with CUR, more reactive oxygen species (ROS) were generated by CCOH and CCN in type I and II synergy upon light irradiation. Cell experiments indicated that CCN with an excellent LD-targeting effect could be used to monitor the changes in the morphology and number of LDs in tumor cells during PDT.

As a natural product, turmeric has been used in traditional medicine for thousands of years and has become a source of ingredients for new medicines.[1] The pharmacological activity of turmeric is mainly attributed to curcumin (CUR),[2] which has a wide range of biological activities, including antioxidant, anti-inflammatory, antibacterial, anticancer, promotion of wound healing, *etc.*[3] In addition, CUR can be used as a photosensitizer (PS) for photodynamic therapy (PDT) because it produces reactive oxygen species (ROS) at 450 nm wavelength excitation.[4] However, the shortcomings of CUR, such as short absorption wavelength, low yields of singlet oxygen ($^1O_2$), and poor stability, limit its application in PDT.[5] How to extend the absorption wavelength[6–8] and enhance the PDT effect of CUR remains a crucial challenge.

The therapeutic effect of PDT is mainly related to the yields of ROS.[9] For type-I PSs, triplet state PSs can react with oxygen and water through electron transfer to generate superoxide anions ($O_2^{-\bullet}$) and hydroxyl radicals ($OH^\bullet$),[10] which enables the complete utilization of the limited amount of oxygen in hypoxic tumors.[11] On the other hand, triplet state PSs can also transfer their energy directly to molecular oxygen (type II), thereby generating cytotoxic $^1O_2$.[12] Type-I PSs rely less on oxygen than type-II PSs because the disproportionation reactions as well as Haber–Weiss/Fenton reactions in type-I PSs will compensate for oxygen.[13] However, hypoxia is a typical feature of the tumor microenvironment and is mainly attributed to abnormal vascular growth and rapid tumor cell proliferation.[14] Therefore, many studies focus on the design and synthesis of type-I and type-II synergistic PSs for PDT in a hypoxic tumor microenvironment.

PDT efficiency is related to not only the types and yields of ROS but also the cellular localization of PSs.[15–17] Lipid droplets (LDs) are phospholipid monolayer spherical organelles containing a variety of neutral lipids and play various roles in numerous cellular processes.[18] Importantly, LDs can provide energy for cancer cells to support their proliferation, invasion, and metastasis, whereas the disruption of LDs can disrupt a number of physiological activities within cells and cause damage to cancer cells,[19,20] which may be potential targets for cancer therapy.[21] In addition, hypoxia can increase the number of LDs in cancer cells and improve the viability of tumor cells.[22] Therefore, the design and synthesis of LD-targeting PSs are a new way to improve the PDT effect.

A number of studies, including those on chemical structure modification,[23] chelating metal ions,[24] and preparation of nanoparticles,[25] have been conducted to overcome the shortcomings of CUR.[26] However, no study reported CUR analogues for LD imaging-guided PDT. Coumarin derivatives have received considerable attention as chemosensors due to their high fluorescence quantum yields and ease of modification. In our previous work, we prepared a series of new fluorescent dyes by the hybridization of coumarin moieties with other dyes, such as rhodamine,[27] fluorescein,[28] and pyronin.[29] In this work, we introduced coumarin into the CUR skeleton to obtain two new PSs (CCOH and CCN) with long wavelengths and high ROS yields (Scheme 1). They can generate $O_2^{-\bullet}$ and $^1O_2$ through type I and II pathways. CCN has more excellent properties in solution, such as a longer absorption wavelength and a higher ROS generation yield, than CCOH. Cell experiments indicated that CCN had an excellent LD-targeting effect and can reduce the survival rate of tumor cells under hypoxic

[a] *Key Laboratory of Photochemical Conversion and Optoelectronic Materials and CityU-CAS Joint Laboratory of Functional Materials and Devices, Technical Institute of Physics and Chemistry, Chinese Academy of Sciences, Beijing, 100190, People's Republic of China. E-mail: wmliu@mail.ipc.ac.cn, wangpf@mail.ipc.ac.cn*
[b] *School of Future Technology, University of Chinese Academy of Sciences, Beijing, 100049, People's Republic of China*
[c] *Institute of Optical Physics and Engineering Technology, Qilu Zhongke, Jinan, 250000, People's Republic of China*

† Electronic supplementary information (ESI) available. See DOI: https://doi.org/10.1039/d2cc07025a

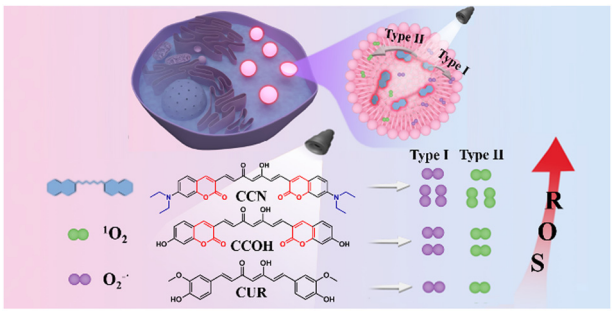

Scheme 1 Chemical structures and illustration of CUR, CCOH, and CCN generated ROS after illumination.

conditions with 532 nm irradiation. Therefore, CCN is expected to become a new LD-targeted PS under hypoxic tumor environments.

The chemical structures and synthetic route of CCOH and CCN are shown in Scheme 1 and Fig. S1 (ESI†). The density functional theory (DFT) calculations showed the energy gaps of CUR, CCOH, and CCN were 3.34, 3.13, and 2.96 eV (Fig. S2, ESI†), which could result in red-shifted absorption and emission. In addition, it can change the exponential distribution coefficient ($C\log P$) of molecules to increase their lipophilicity. CCOH and CCN were characterized by ^{1}H NMR, ^{13}C NMR, and MS. The results are shown in Fig. S3–S8 (ESI†).

Fig. 1a and b shows the normalized UV-Vis absorption and fluorescence spectra of CUR, CCOH and CCN, respectively. Compared with CUR, compound CCOH extended the conjugated chain by introducing a lactone ring, but it had a weaker electron-donating group (hydroxyl) than that of CUR (methoxy), which weakened the D–A effect. Thus, the red shift of CCOH in the absorption wavelength was small (16 nm). CCN replaced the weak electron-donating group (hydroxyl) with the strong electron-donating group (diethylamine), which greatly enhanced the D–A effect, resulting in a larger red shift in absorption and fluorescence spectra than CUR. The maximum absorption and fluorescence wavelengths of CCN in DMSO were 537 nm and 625 nm.

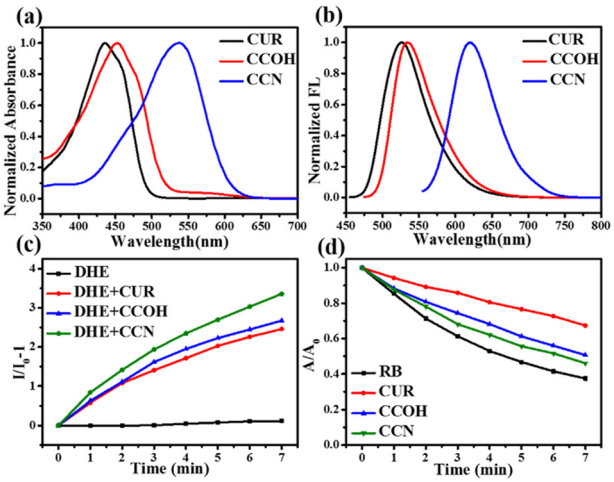

Fig. 1 (a) Normalized absorption spectra of CUR, CCOH and CCN in DMSO. (b) Normalized fluorescence spectra of CUR (λ_{ex}: 435 nm), CCOH (λ_{ex}: 451 nm) and CCN (λ_{ex}: 537 nm) in DMSO. (c) Relative changes in fluorescence emission intensity at 610 nm of DHE (λ_{ex}: 510 nm) in the presence of CUR (20 μM), CCOH (20 μM), and CCN (20 μM) under xenon lamp irradiation (0.05 W cm^{-2}). (d) The degradation rate of ABDA (50 μM) at 378 nm in the presence of RB, CUR, CCOH and CCN under xenon lamp irradiation (0.05 W cm^{-2}).

In addition, the solvent effects of CUR, CCOH, and CCN were studied (Fig. S9–S11, ESI†). Fig. S11b (ESI†) shows that, with the increase of solvent polarity, the fluorescence spectrum of CCN exhibited an evident red shift from 545 nm to 625 nm, which indicates that CCN has an intramolecular charge transfer effect. Tables S1–S3 (ESI†) list the maximum absorption and emission wavelengths, fluorescence quantum yields, Stokes shifts, and molar extinction coefficients of CUR, CCOH, and CCN. The results showed that CCN has a long absorption wavelength and a high fluorescence quantum yield (0.62) in medium-polarity solvents close to lipids (Table S3, ESI†).

The ROS production capability of the three compounds was detected. Given the different absorption wavelengths of the three compounds, a xenon lamp was selected as the light source. Dihydroethidium (DHE) was selected as the $O_2^{-\bullet}$ probe. Fig. 1c and Fig. S12 (ESI†) show that the $O_2^{-\bullet}$ generation capability of CUR, CCOH, and CCN increased in turn. For detecting the $^1O_2$ yield, Rose Bengal was selected as the reference and 9,10-anthracenediyl-bis (methylene) dimalonic acid (ABDA) as the detection probe for $^1O_2$. As shown in Fig. 1d and Fig. S13 (ESI†), the $^1O_2$ yields of CUR, CCOH, and CCN after irradiation were 5.11%, 11.87% and 23.88%, respectively. Importantly, CCN can produce more ROS under xenon lamp irradiation than CCOH. Thus, CCN was selected for further experiments due to its highly effective ROS generation capability, long-wavelength absorption, and deep-red emission.

Considering that a laser is often used as the light source in clinical PDT, we selected a 532 nm laser as the light source to test the ROS generation of CCN. CCN had a relatively stable $O_2^{-\bullet}$ and $^1O_2$ production capacity (Fig. S14 and S16, ESI†), and it is expected to be used in hypoxic tumor microenvironment PDT. In addition, the $^1O_2$ yield of CCN under 532 nm laser irradiation is 0.27 (Fig. S18 and S19, ESI†). As shown in Fig. S20 (ESI†), CCN generated ROS under 532 nm laser irradiation by electron spin resonance spectroscopy, which further confirmed that CCN can generate $O_2^{-\bullet}$ and $^1O_2$. In addition, the photostability and pH effect of CCN were investigated (Fig. S21, ESI†). All the results observed in solution showed that CCN resulted in high fluorescence yield, large Stokes shift, good photostability, and excellent pH stability, which can be promising for fluorescence imaging-guided PDT.

To explore the bioimaging capability of CCN, we incubated HepG-2, HeLa, and 4T1 cells with this compound. Confocal laser scanning microscopy (CLSM) imaging showed that CCN can penetrate the cell membrane by diffusion and displayed evident fluorescence in the red channel at 1 h (Fig. S22, ESI†). More importantly, given that the cell membrane is a bilayer lipid structure, lipophilic compounds easily passed through the cell membrane and accumulated in LDs within the cells. According to previous literature,[30] compounds with $C\log P >$ 5 usually exhibit LD targeting. CCN has a $C\log P$ value of 6.57,

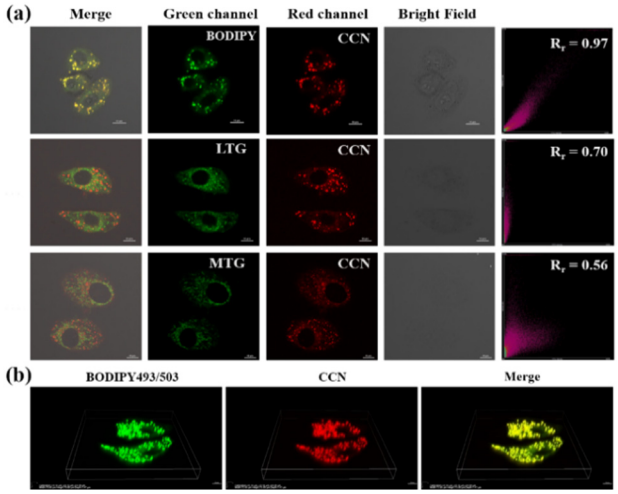

Fig. 2 (a) CLSM images of CCN (2 μM) colocalized with BODIPY (0.5 μM), MTG (0.2 μM), and LTG (0.2 μM) in HepG-2 cells. Scale bar: 10 μm. (b) 3D reconstructed image of CCN (2 μM) colocalized with BODIPY (0.5 μM) in HepG-2 cells. Scale bar: 10 μm.

which indicates good lipophilicity and conduciveness to penetrating cell membranes and targeting LDs (Fig. S2, ESI†).

To explore the subcellular location of CCN in live cells, we selected commercial probes, such as BODIPY 493/503 (BODIPY), MitoTracker Green (MTG), and LysoTracker Green (LTG), as controls. As shown in Fig. 2a, CCN red channel fluorescence and BODIPY green channel fluorescence can be observed, and the merged images overlapped well. The Pearson correlation coefficient (R_r) was 0.97, which was considerably higher than those of other organelles (mitochondrial: 0.56, lysosome: 0.70). As shown in Fig. S23 (ESI†), the fluorescence channels of BODIPY and CCN in HepG-2 cells do not interfere with each other. R_r values were both 0.95 in HeLa and 4T1 cells (Fig. S24 and S25, ESI†), which indicated that CCN has a powerful LD-specific targeting capability.

In the three-dimensional (3D) reconstructed image (Fig. 2b), spherical LDs of different sizes in HepG-2 cells can be observed in the red channel, which completely overlapped with the green fluorescence of BODIPY. The experimental results showed that CCN has good lipophilicity and permeability to cell membranes and is more likely to be enriched in LDs. As shown in Fig. S26 (ESI†), the fluorescence intensity of CCN remained unchanged, and that of BODIPY decreased significantly to about 40%, indicating that CCN has good photostability.

We designed the experiment to demonstrate ROS generation of CCN using oleic acid (OA) to simulate LDs. As shown in Fig. S27 (ESI†), the fluorescence intensity increased with the prolongation of illumination time, which indicates that CCN can produce ROS in lipid environments. To further explore whether CCN can generate $O_2^{-\bullet}$ in live cells, we used DHE to capture the $O_2^{-\bullet}$ produced by CCN after irradiation with a 532 nm laser. As shown in Fig. S28 and S29 (ESI†), the red fluorescence of CCN showed an irregular droplet distribution in the cytoplasm, whereas the red fluorescence generated by $O_2^{-\bullet}$ combined with DHE was evenly distributed in the cytoplasm and entered the nucleus, which implied that CCN can continuously and stably produce $O_2^{-\bullet}$ in normoxia or hypoxia. The $^1O_2$ probe singlet oxygen sensor Green was used to monitor the process of CCN in generating $^1O_2$ after irradiation. With the prolonged irradiation time, the intracellular fluorescence gradually increased, indicating the gradual increase in intracellular $^1O_2$ (Fig. S30, ESI†).

CCN can simultaneously generate two kinds of ROS in cells, which increases the killing ability of tumor cells. To further explore the damage of CCN to LDs under 532 nm laser irradiation, we used a laser to irradiate HepG-2 cells containing CCN and captured images every 4 min to observe the changes in LDs during PDT. In the control group without laser irradiation (Fig. 3a), the cell morphology and the number of LDs in cells did not change significantly. As shown in Fig. 3b, with the extension of irradiation time, the cells in the experimental group gradually died and the red fluorescence of LDs gradually decreased (Fig. 3c), which indicated that CCN has an excellent PDT effect by targeting LDs.

We used the thiazolyl blue tetrazolium bromide (MTT) assay to evaluate the PDT effect of CCN on HepG-2, HeLa, and 4T1 cells. As shown in Fig. 4a and Fig. S31 (ESI†), under dark conditions, CCN had no evident cytotoxicity toward HepG-2, HeLa, and 4T1 tumor cells (at 10 μM, the cell viability was higher than 80%). Under 532 nm laser irradiation, all three tumor cells exhibited dose-dependent cytotoxicity, and the cytotoxicity increased significantly with the increase in the concentration of CCN. The calculated IC50 values of CCN for

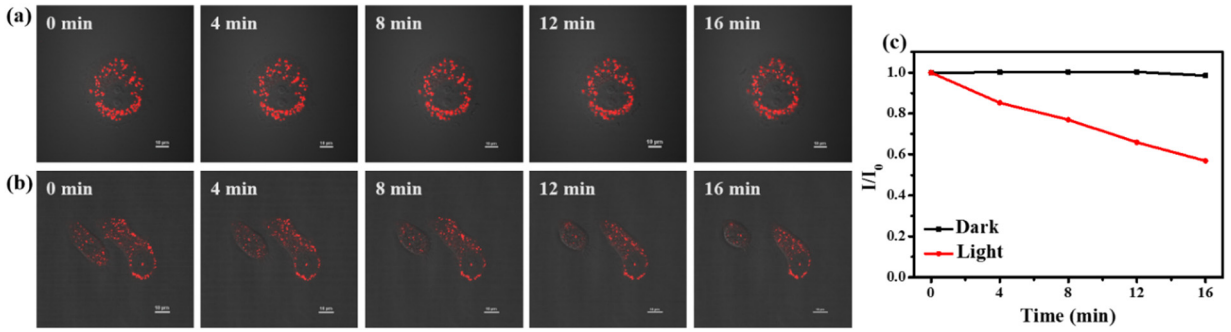

Fig. 3 (a) CLSM images of HepG-2 cells after being incubated with CCN (5 μM) without laser irradiation. Scale bar: 10 μm. (b) CLSM images of HepG-2 cells after being incubated with CCN (5 μM) irradiated with a 532 nm laser (0.02 W cm^{-2}) every 4 min. Scale bar: 10 μm. (c) Relative changes in the mean fluorescence intensity of control and experimental groups in the red channel.

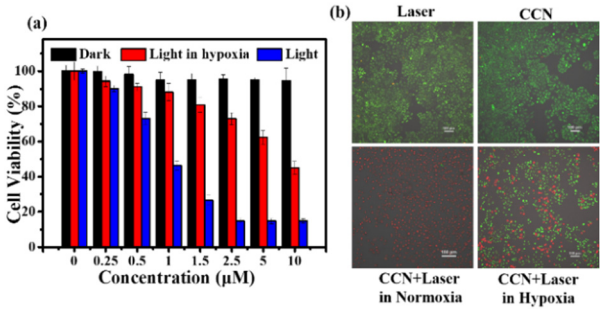

Fig. 4 (a) Cell viability of HepG-2 cells after being incubated with different concentrations of CCN with irradiation of a 532 nm laser (0.1 W cm^{-2}) for 10 min. (b) CLSM images of HepG-2 cells after being incubated with CCN (2.5 μM) and AM/PI upon irradiation with a 532 nm laser (0.1 W cm^{-2}) for 10 min. Scale bar: 100 μm.

HepG-2, HeLa, and 4T1 cells are shown in Table S4 (ESI†). Under hypoxic conditions, CCN damaged the cancer cells by producing $O_2^{-\bullet}$. In air, the cytotoxicity of CCN was more pronounced because the two mechanisms synergized to generate ROS, which caused damage to tumor cells.

To further verify the PDT effect of CCN on HepG-2 cells, we used calcein AM and propidium iodide (AM/PI) cell activity and cytotoxicity assays to detect such influence. As shown in Fig. 4b, cells in the light-only and the CCN-only groups showed strong green fluorescence, which indicated the good biocompatibility of CCN. In the experimental group after CCN irradiation, almost all tumor cells were killed. In the experimental group under hypoxic conditions, several cells died, consistent with the findings of the MTT assay. The experimental results showed that CCN is expected to be used in hypoxia PDT guided by LD imaging due to its good biocompatibility and high phototoxicity.

In summary, we designed and synthesized two PSs based on the CUR skeleton. By introducing coumarin moieties and strong electron-donating groups, CCOH and CCN not only solved the shortcomings of the short absorption wavelength and low fluorescence quantum yield of CUR, but also greatly improved the ROS generation. Moreover, CCN with an excellent LD-targeting effect could be used to monitor the changes in the morphology and number of LDs in tumor cells during PDT. The evident phototoxicity of CCN was achieved in a hypoxic tumor microenvironment due to its ROS generation through type I and II pathways. This work provides a new idea for improving the shortage and utilization of natural CUR.

This work was supported by the National Natural Science Foundation of China (No. 61720106014, 21873110, and 62005294) and the Key Research Program of Frontier Sciences, CAS (Grant No. QYZDJSSW-JSC032).

Conflicts of interest

There are no conflicts to declare.

Notes and references

1 A.-E. Segneanu, G. Vlase, A. T. Lukinich-Gruia, D.-D. Herea and I. Grozescu, *Antioxidants*, 2022, **11**, 2261.
2 H. Mirzaei, A. Shakeri, B. Rashidi, A. Jalili, Z. Banikazemi and A. Sahebkar, *Biomed. Pharmacother.*, 2017, **85**, 102–112.
3 S. Hasanzadeh, M. I. Read, A. R. Bland, M. Majeed, T. Jamialahmadi and A. Sahebkar, *Pharmacol. Res.*, 2020, **159**, 104921.
4 Y. Lan, X. Zhu, M. Tang, Y. Wu, J. Zhang, J. Liu and Y. Zhang, *Nanoscale*, 2020, **12**, 7875–7887.
5 L. Xie, X. Ji, Q. Zhang and Y. Wei, *Biomed. Pharmacother.*, 2022, **146**, 112567.
6 J. Wu, C. Shao, X. Ye, X. Di, D. Li, H. Zhao, B. Zhang, G. Chen, H. K. Liu and Y. Qian, *ACS Sens.*, 2021, **6**, 863–870.
7 N. R. Paisley, S. V. Halldorson, M. V. Tran, R. Gupta, S. Kamal, W. R. Algar and Z. M. Hudson, *Angew. Chem., Int. Ed.*, 2021, **60**, 18630–18638.
8 D. Shi, L. Hu, X. Li, W. Liu, Y. Gao, X. Li, B. Jiang, C. Xia, Y. Guo and J. Li, *Sens. Actuators, B*, 2020, **319**, 128302.
9 J. Dang, H. He, D. Chen and L. Yin, *Biomater. Sci.*, 2017, **5**, 1500–1511.
10 T. Luo, K. Ni, A. Culbert, G. Lan, Z. Li, X. Jiang, M. Kaufmann and W. Lin, *J. Am. Chem. Soc.*, 2020, **142**, 7334–7339.
11 C. Zhang, W.-J. Qin, X.-F. Bai and X.-Z. Zhang, *Nano Today*, 2020, **35**, 2261.
12 J. An, S. Tang, G. Hong, W. Chen, M. Chen, J. Song, Z. Li, X. Peng, F. Song and W. H. Zheng, *Nat. Commun.*, 2022, **13**, 2225.
13 M. Li, T. Xiong, J. Du, R. Tian, M. Xiao, L. Guo, S. Long, J. Fan, W. Sun, K. Shao, X. Song, J. W. Foley and X. Peng, *J. Am. Chem. Soc.*, 2019, **141**, 2695–2702.
14 Y. Wan, L. H. Fu, C. Li, J. Lin and P. Huang, *Adv. Mater.*, 2021, **33**, e2103978.
15 X. Chen, Y. Zhang, X. Zhang, Z. Zhang and Y. Zhang, *Mikrochim. Acta*, 2021, **188**, 349.
16 X. Guo, N. Yang, W. Ji, H. Zhang, X. Dong, Z. Zhou, L. Li, H. M. Shen, S. Q. Yao and W. Huang, *Adv. Mater.*, 2021, **33**, e2007778.
17 L. C. Gomes-da-Silva, L. Zhao, L. Bezu, H. Zhou, A. Sauvat, P. Liu, S. Durand, M. Leduc, S. Souquere, F. Loos, L. Mondragon, B. Sveinbjornsson, O. Rekdal, G. Boncompain, F. Perez, L. G. Arnaut, O. Kepp and G. Kroemer, *EMBO J.*, 2018, **37**, e98354.
18 F. Zhang, Y. Liu, B. Yang, P. Guan, J. Chai, G. Wen and B. Liu, *J. Mater. Chem. B*, 2021, **9**, 2417–2427.
19 W. Zhuang, P. Tan, S. Li, C. Li, J. Zhang, J. Ai, L. Yang, G. Li, Q. Wei, M. Chen and Y. Wang, *J. Mater. Chem. B*, 2021, **9**, 9553–9560.
20 P. Tan, W. Zhuang, S. Li, J. Zhang, H. Xu, L. Yang, Y. Liao, M. Chen and Q. Wei, *Chem. Commun.*, 2021, **57**, 1046–1049.
21 X. Xu, G. Deng, Z. Sun, Y. Luo, J. Liu, X. Yu, Y. Zhao, P. Gong, G. Liu, P. Zhang, F. Pan, L. Cai and B. Z. Tang, *Adv. Mater.*, 2021, **33**, e2102322.
22 X. Li, W. Xu, Z. Yang, S. Li, X. Gu, T. Yuan, C. Li, Y. Wang and J. Hua, *Sens. Actuators, B*, 2023, **375**, 132892.
23 S. N. Margar and N. Sekar, *J. Photochem. Photobiol., A*, 2016, **327**, 58–70.
24 A. Colombo, M. Fontani, C. Dragonetti, D. Roberto, J. A. G. Williams, R. Scotto di Perrotolo, F. Casagrande, S. Barozzi and S. Polo, *Chemistry*, 2019, **25**, 7948–7952.
25 J. Wang, M. Zheng and Z. Xie, *J. Colloid Interface Sci.*, 2019, **535**, 84–91.
26 M. Khudhayer Oglah and Y. Fakri Mustafa, *Med. Chem. Res.*, 2019, **29**, 479–486.
27 J. Chen, W. Liu, B. Zhou, G. Niu, H. Zhang, J. Wu, Y. Wang, W. Ju and P. Wang, *J. Org. Chem.*, 2013, **78**, 6121–6130.
28 S. Qi, Q. Li, W. Liu, H. Ren, H. Zhang, J. Wu, J. Ge and P. Wang, *Spectrochim. Acta, Part A*, 2018, **204**, 590–597.
29 B. Zhou, W. Liu, H. Zhang, J. Wu, S. Liu, H. Xu and P. Wang, *Biosens. Bioelectron.*, 2015, **68**, 189–196.
30 Y. Dai, X. Zhao, H. Ji, D. Zhang, P. Zhang, K. Xue, S. Misal, H. Zhu and Z. Qi, *Chem. Eng. J.*, 2021, **410**, 128186.

